Modeling the seismic response of basin-edge structure by a sequential waveform method

Lian-Feng Zhao *, Wei-Min Wang, Juan Li, Zhen-Xing Yao

Institute of Geology and Geophysics, CAS, Beijing, China

Abstract

A sequential waveform method is developed to simulate the seismic response of basin-edge structure excited by a plane incident P-wave. The full procedure involves: (a) a previous parameterization of the investigated model using the seismic wave velocities and depths of the sedimentary stratifications; (b) an input motion determined from the records at stations installed on hard rock; (c) forward computation of the P-SV elastic wave field by means of a two-dimensional finite difference (FD) method; (d) the optimization of the model vector using simulated annealing technique and comparing the simulated seismic response of the tested structure with the observed wave field; (e) the correction of the initial model by trial-and-error by testing the differences between synthetics and observed data, and (f) the final solution obtained by iteration using the conjugate gradient algorithm. The search of an optimal basin-edge model has been parallel processed by varying the shapes and velocities of strata on the basis of the fitting of relative timing, amplitude and phase between the output and the observed data. The input motion and sensitivity have been checked and the validity of the method has been demonstrated by numeric analysis. Using the teleseismic records generated by 7 earthquakes recorded at 26 broadband seismic stations, we have studied the seismic velocity structure of the southern edge of the Jiyang depression located in the Bohai Bay basin, northern China. Two cross sections show an agreement between the velocity results and the geological sections available in the region. In addition, we obtain evidence of three hidden faults under the sections and features that suggest major extensions at the Paleogene.
© 2006 Elsevier B.V. All rights reserved.

1. Introduction

Since the earthquake damage associated with sedimentary basins is more severe than other forms, it is important in seismic hazard analysis to evaluate the effects of basin structure on the propagation of seismic energy (Anderson et al., 1986; Campillo et al., 1989; Kawase and Aki, 1989). The amplification effect of

basin structure on shear wave amplitude, which usually leads to undesirable damage, has been investigated by Kebeasy and Husebye (2003a,b). On the other hand, because the sedimentary basins are related to oil-bearing structure (Zhang et al., in review), it is necessary to clearly understand the basin structure in order to investigate the genetic types, tectonic systems and geodynamic models of oil- and gas-bearing basins (Ye et al., 1987; Hou et al., 2001). Although the superficial structure of sedimentary basins can be generally prospected by the available seismic means, the interior structure has to be evaluated via observation of

---

* Corresponding author. Tel.: +86 10 62007370; fax: +86 10 62010846.

E-mail address: zhaolf@mail.igcas.ac.cn (L.-F. Zhao).

earthquakes. Several studies have been performed to understand the subsurface structure by waveform data from earthquakes, in the Los Angeles basin (Scrivner and Helmberger, 1994; Olsen et al., 1995; Magistrale et al., 1996; Hauksson and Haase, 1997; Wen and Helmberger, 1997; Wald and Graves, 1998; Ji et al., 2000), the Volvi basin in Northern Greece (Jongmans et al., 1998; Riepl et al., 1998), the Parkway Basin in New Zealand (Duggan, 1997; Chávez-García et al., 1999; Stephenson, 2000; Chávez-García, 2003) and the Bohai Bay basin in Northern China (Zhao et al., 2004).

In general, there are several methods to estimate the geological structure on the basis of the seismic wave propagation, i.e., the refraction/reflection methods, the receiver function method and the waveform inversion. Since the refraction method uses arrival time data, its application is limited to the regions underlaying the observation sites. The reflection method is expensive due to the need of artificial sources and quality records. The source strength also limits the depth that the method can reach (Aio et al., 1997). The receiver function method is mainly used in the case of parallel or gradient layers (Langston, 1977, 1979; Owens et al., 1984; Liu et al., 1996; Yuan et al., 2000), but not when the medium has undulating interfaces such as the basin-edge structure. The seismic waveform inversion is appropriate to investigate a subsurface regional structure from observations coming from a sparse set of stations. This method has been employed by Beck and Hall (1986), Kawase and Aki (1989), Yamanaka et al. (1989), Scrivner and Helmberger (1994), Aio et al. (1995, 1997) and Ji et al. (2000). However, all these works concern the SH system. As we know, the P-SV waveforms are more complicated to analyze because of the energy conversion between P- and S-waves at basin interfaces. Wen and Helmberger (1998) used a two-dimensional P-SV hybrid method to model the local structure near the core–mantle boundary. Based on their approach, we have developed a sequential waveform method to simulate the seismic response and reconstruct the velocity structure of the basin-edge using teleseismic data.

The Northern China Interior Structure Project (NCISP), conducted by the Institute of Geology and Geophysics, Chinese Academy of Sciences, during the period from September 2000 to March 2003, has resulted in large-scale observations on the Bohai Bay basin. High-quality teleseismic data were collected from densely-distributed portable stations. Zhao et al. (2004) have made previous work about the south-edge structure of the Jiyang depression considering the teleseismic SH wave response. P-wave multiples and P-to-S conversions from the sedimentary stratifications see that the P-SV waveform recordings contain more information on basin structure than SH. We consequently focus on the P-SV wave response and develop a sequential waveform method with the same target.

2. Elastic wave field computation

2.1. 2D FD method for P-SV wave field extrapolation

The P-SV wave propagation problem is graphically illustrated in Fig. 1. Although the seismic responses of the basin structure are various and complicated, they can be expressed by a number of individual operators (Wen and Helmberger, 1997; Ji et al., 2000). Specifically, the synthetic seismogram $f_i(t)$, a motion component at station i, is given by the source excitation $S(t)$, instrumental impulse response $I(t)$, deep earth response
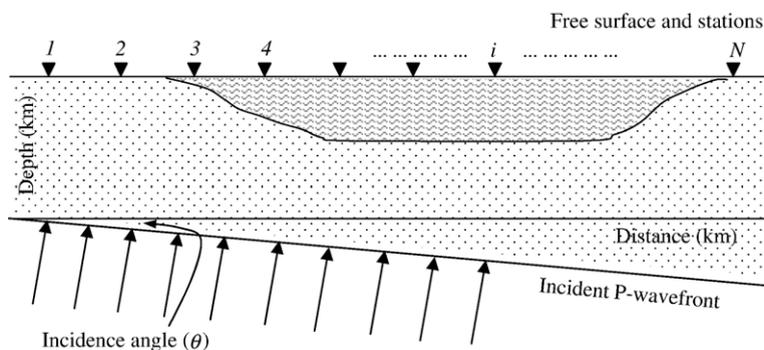

Fig. 1. This illustration shows schematically a basin-edge structure consisting of a sedimentary cover overlaying a homogeneous basement, which is monitorized by seismic receivers (from 1 to N) placed at the free surface. The excitation of the elastic medium is due to the incidence of a plane P-wave with angle θ that is calculated by the ray parameter. The input motion is extrapolated from the coseismic displacement recorded at a hard rock station (1 or 2 on the left). We are interested in the near-surface structure response to the incident wavefront by means of a 2D FD method for P-SV wave field computation.

$E_{far}(t)$ and the "site response" $E_{near\ i}(t)$ in the course of the energy propagation from the source to the station i, and it is expressed by the convolution product:

$$f_i(t) = S(t)*E_{far}(t)*E_{near\ i}(t)*I(t), \qquad (1)$$

where the site response $E_{near}(t)$ is our main interest in this paper. To perform P-SV wave field propagation calculation, we have to select teleseismic events located approximately in line with the station array. Because the stations are sufficiently far away from the source, we can consider the P-wave as a plane wave with a small incident angle. Assuming that the j-th station is placed on hard rock outside of the basin, the site response $E_{near\ j}(t)$ is the retarded time term of the incident P-wave from the bottom of the Earth's crust, which can be expressed as

$$E_{near\ j}(\omega) = e^{-i\omega\Delta t_p}, \qquad (2)$$

where Δt_p is the retarded time computed by

$$\Delta t_p = (h/\cos\theta + (x_j - h\cdot\tan\theta)\cdot\sin\theta)/V_p, \qquad (3)$$

where h indicates the depth of the tested region (Fig. 1), x_j is the location of the j-th station, θ is the plane wave incident angle, and V_p is the average velocity of the basement medium. From Eq. (1), we can obtain the expression in the frequency domain for the seismogram at the j-th station:

$$f_j(\omega) = S(\omega)\cdot E_{far}(\omega)\cdot e^{-i\omega\Delta t_p}\cdot I(\omega). \qquad (4)$$

If the i-th station is located in the basin, the seismogram in the frequency domain can be expressed as

$$f_i(\omega) = S(\omega)\cdot E_{far}(\omega)\cdot E_{near\ i}(\omega)\cdot I(\omega). \qquad (5)$$

From Eqs. (4) and (5), we have

$$f_i(\omega) = f_j(\omega)\cdot e^{i\omega\Delta t_p}\cdot E_{near\ i}(\omega). \qquad (6)$$

Returning to the time domain, we obtain

$$f_i(t) = f_j(t-\Delta t_p)*E_{near\ i}(t). \qquad (7)$$

Eq. (7) gives the seismogram observed at a basin station, which is expressed by the convolution of the seismogram observed at a hard rock station outside the basin with the site response function. Therefore, the input motion $U_{inc}(t)$ in a FD scheme for the P-SV wave field, can be determined from the records observed at the hard rock stations outside the basin:

$$U_{inc}(t) = f_j(t-\Delta t_p). \qquad (8)$$

In the FD calculation of the P-SV wave field propagation, the basin model is described by iso-velocity layers depicted by dipping segments defined by equidistant depth points (solid circles in Fig. 2a). In other words, the basin model vector $\mathbf{m}$ is a function of the layer velocities and the points describing geological interfaces:

$$\mathbf{m} = (V_s(l),\ V_p/V_s(l), \mathbf{P}(k))$$
$$(l = 1, 2, \cdots, L; k = 1, 2, \cdots L). \qquad (9)$$

Here, $V_s(l)$ and $V_p/V_s(l)$ express the S-wave velocity and the Poisson ratio between P-wave velocity and S-wave velocity for the l-th layer, respectively. L is the number of geological layers. $\mathbf{P}(k)$ is a point set that describes the k-th interface, and can be expressed by means of adjustable control depths

$$\mathbf{P}(k) = h(\Delta x\cdot(i-1), k), i = 1, 2...N, \qquad (10)$$

where Δx is the step for horizontal distance and N is the control depth point number for the k-th layer. In our elastic FD scheme, geometrically averaged parameters are employed (Zahradník, 1995), fourth-order difference in space and second-order difference in time are applied in the interior of the probed region, and second-order differences in both space and time are used at the grid points of the boundary. On the left, right and bottom boundaries, we have applied the absorbing conditions of Clayton and Engquist (1977).

2.2. Input motion

Numeric tests are performed to validate the input motion obtained from Eq. (8). To do that, a geological model similar to the structure of our interest is designed, and the following steps are addressed:

1) Assumption of the incident plane P-wave:

$$U_{inc}(t) = (2\pi^2 f_0^2 t^2 - 1)\exp(-\pi^2 f_0^2 t^2), \qquad (11)$$

where f_0 is the predominant frequency.
2) Computation of the vertical and horizontal motion components at the surface receivers using a 2D FD method for the P-SV wave field propagation and the assumed input.
3) Computation of the input motion by Eq. (8).
4) Comparison of the computed input motion with the assumed input.
5) Computation of the surface motion using the FD method and the computed input motion.
6) Comparison of the surface motions given by the two inputs.

Fig. 2a shows a four-layer basin-edge structure model with a relatively large velocity contrast between elastic layers, where the layer parameters are labeled. The FD calculations are conducted with a grid step of 0.2 km ($\Delta x = \Delta z = 0.2$ km), a time step of 0.025 s ($\Delta t = 0.025$ s) and plane P-wave incident angle of 20° ($\theta = 20°$). Curves 1, 2 and 3 in Fig. 2b show the time history of $U_{inc}(t)$ and the corresponding input motion computed from Eq. (8) respectively. A good agreement in both timing and waveform has been found between the assumed input

(a) Basin model
(b) Inputs
(c) Vertical components
(d) Horizontal components

motion and the calculated one. Another comparison is made from the seismograms at surface stations. The vertical and radial records are shown in Fig. 2c and d, where the stations are evenly spaced at a distance of 6.0 km, and the solid lines and dashed ones are the results computed from the assumed input signal $U_{inc}(t)$ and the calculated input motion $f(t - \Delta t_p)$, respectively. The results too display a good agreement in both timing and waveform. Therefore, we conclude that the method to gain the input motion is valid.

In addition, we investigate the P-SV wave field synthetics through the snapshot displays (Fig. 3), which represent the basin model excited by a plane incident P-wave. At small lapse times, it is easy to recognize the plane wave and its reflection on the surface in both vertical (Fig. 3a) and horizontal (Fig. 3b) displacements. For lapse times exceeding 4 s the plane wavefront enters into the basin and the synthetic wave field becomes complex. This is due to the reverberation of the conversions on the geological interfaces and the multiple reflections within each stratum. The reverberation effect also produces wave field amplification and a large coda amplitude (Kebeasy and Husebye, 2003a). This implies that the observed data of the P-SV wave field can be used to infer structural features of a basin-edge.

2.3. Sensitivity tests

This type of test is necessary in order to know more about the physical relationship between the model complexity and the observed motions. For this purpose, a synthetic two-layer model is considered: the lower layer is a basement uplift and the upper one is a depression (Fig. 4a). The test model displays a basin-edge structure, which is expressed by a simple layer parameterized by control depth points with a 5.0 km horizontal interval. The basin-edge is excited by an
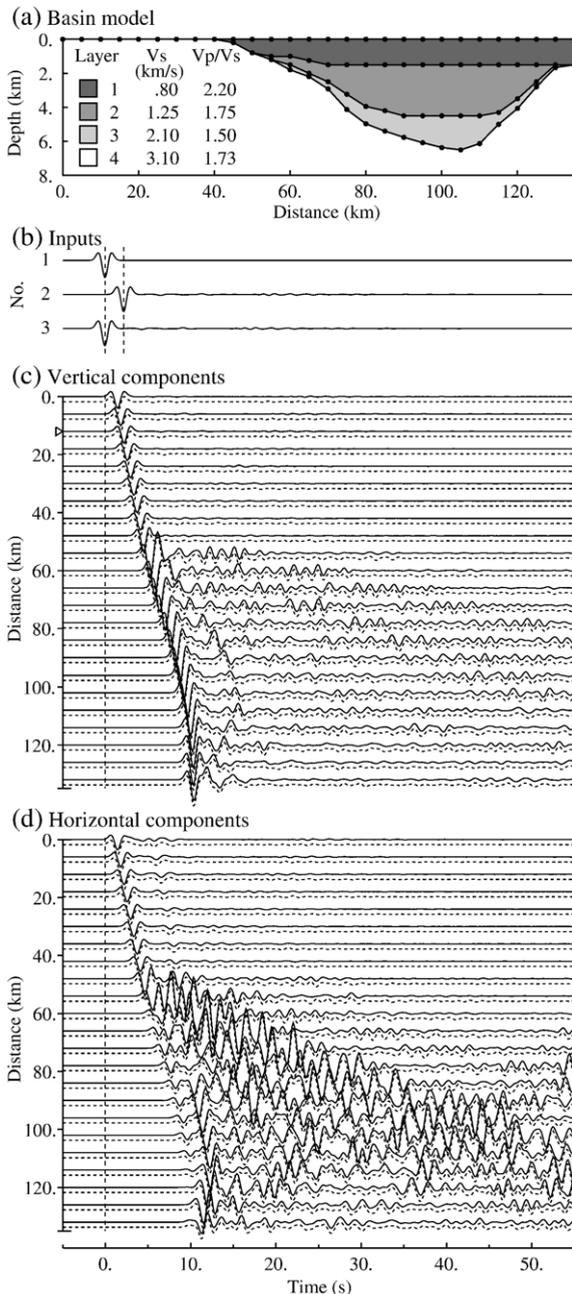
Fig. 2. Four-layer basin-edge structure model considered to carry out numerical simulations for checking the validity of the FD calculation of the extrapolated P-SV wave field when a plane P-wave recorded at a hard rock station is taken as input motion. (a) Parameterized basin model by S-wave velocity (V_s) and Poisson ratio (V_p/V_s) for each stratum. The surface station array is evenly spaced 6.0 km. Black points evenly spaced 5.0 km horizontally are control depth points defining the interfaces that configure the geometry of the model. (b) Trace 1 is the assumed input motion; trace 2 is the synthetic vertical component record at the station on hard rock marked by a triangle in (c); trace 3 is the input motion computed by Eq. (8) from curve 2, which shows its coincidence with the assumed input motion (curve 1). (c) Synthetic seismograms showing the vertical component of the ground motion obtained using either the assumed input motion (continuous line traces) or the calculated input motion (dash line traces). (d) Synthetic seismograms for the radial component of the ground motion obtained by the two ways.
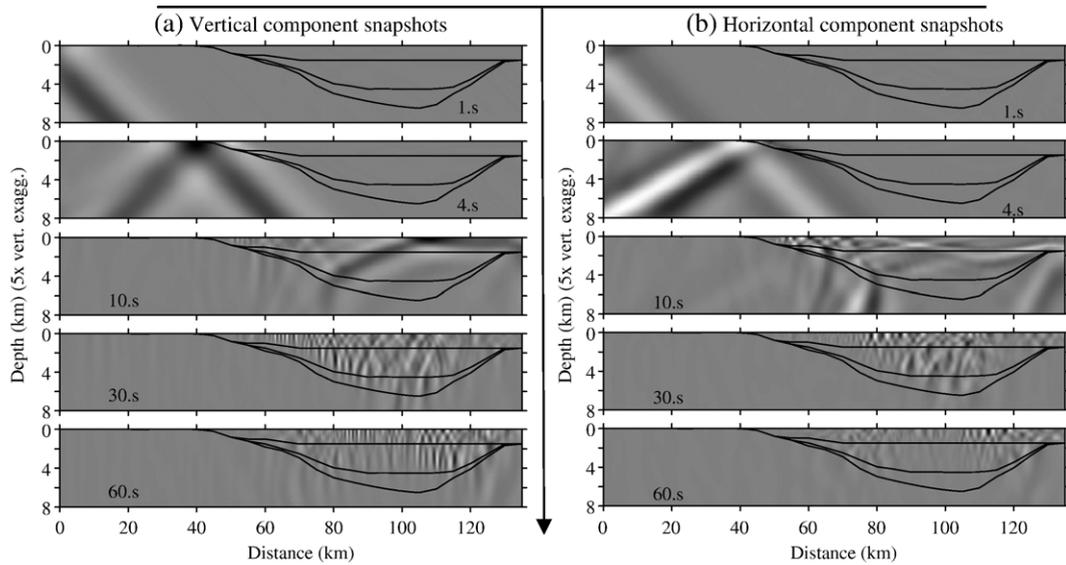
Fig. 3. A series of snapshots for lapse times increasing from 1 to 60 s, showing the wave propagation across the basin model described in Fig. 2a: (a) panels for vertical displacements; (b) panels for horizontal displacements. The input motion is the same that before (trace 1 in Fig. 2b).

input motion calculated from the record at station 076MZ (listed in Table 1) due to event ep04705 (listed in Table 2).

To describe the sensitivity of the observed waveforms to changes in the physical model, a correlation function, containing waveform fitting and travel time constraint (Ji et al., 2000), is introduced to evaluate the similarity between synthetic and observed seismograms:

$$g(\tau) = 1.0 - 2 \frac{\int f_{obs}(t) f_{syn}(t + \tau) dt}{\int (f_{obs}^2(t) + f_{syn}^2(t + \tau)) dt}, \quad (12)$$

where $f_{obs}(t)$ and $f_{syn}(t)$ are the observed and synthetic seismograms, respectively, and τ is the time shift between them. If the synthetic seismograms fit the observed data perfectly in both timing and waveform, the time shift τ is 0 and the correlation function $g(\tau)$ is also 0. Hence, for two congruent waveforms, the time shift, if any, can be determined by Eq. (12) with $g(\tau)$ equal to 0. Generally, neither waveforms are congruent, nor the time interval is zero. However, once the best fitting waveform is found, τ can be determined with a scatter value of $\delta\tau$ by minimizing the correlation coefficient within the possible time range, i.e.,

$$g(\delta\tau) = \min\{g(\tau), \tau \in [-T, T]\}, \quad (13)$$

where T is the estimated maximum travel time difference between the observed and calculated seismograms.

Fig. 4a shows the sedimentary basin model, where the model parameters are included. The solid circles represent the control depth points, by which an initial

model is defined. As numeric examples, three local variation models, called Model A, Model B and Model C and depicted by dashed lines in Fig. 4a, were constructed raising either the point A or the point B or the two at the same time, respectively. We have used the FD method to generate synthetics based on the initial and generated models. The vertical and radial displacements are displayed in Fig. 4b and c, respectively. The solid lines represent the seismic responses of the initial model, while the dashed lines come from a rise of 2.5 km of the point A. It is found that this rise results in a time difference of 1.35 s and a waveform misfit of 3.88 between the initial model and Model A. Fig. 5a shows the differences of the seismic responses caused by the three local variation models with different heights. The solid lines represent the time residuals while the dashed lines correspond to the waveform misfit. The solid circle, the solid triangle and the cross in the lines refer to Model A, B and C, respectively. Both time residual and waveform misfit increase with the rise of the control points. Models A and C give similar variations in time, albeit Models A and B give similar variations in waveforms, although different from those supplied by Model C. Fig. 5b shows the time residuals and waveform misfits of the vertical and radial motion components at each station as a result of a shift of 2.5 km of the point A. Similarly, Fig. 5c and d provide these results for Models B and C, respectively. It is noted that the seismic response difference reaches the maximum at the station (No. 10) just located above the moving points. This implies that the near-receiver structure
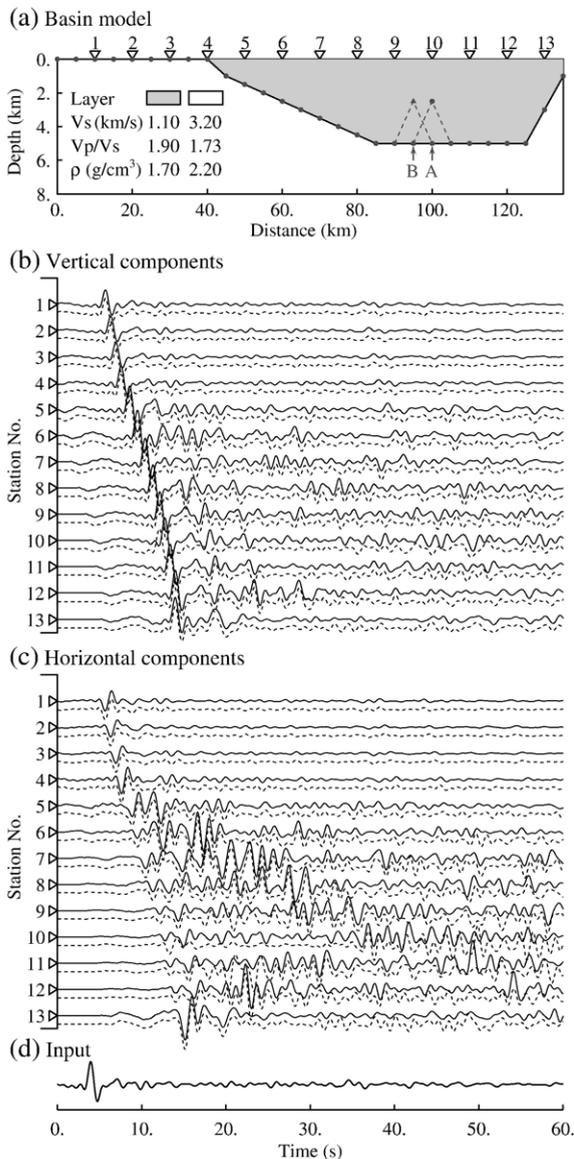
Fig. 4. A sample two-layer basin model considered to carry out several sensitivity tests through the computation of synthetic from local structural variations. These local changes come from the hypothesized displacement (2.5 km) of a single control depth point up (A or B in the plot, dashed lines), or else from the displacement of two points (A and B) simultaneously. (a) Parameterized model by S-wave velocity (V_s), Poisson ratio (V_p/V_s) and density (ρ) for each stratum. The structure is theoretically monitorized by 13 seismic stations (triangles) evenly spaced 10 km at surface. Black points evenly spaced 5.0 km horizontally are control depth points defining the single interface in the model. (b and c) Synthetic seismograms at surface stations showing the vertical (b) and radial (c) components of the ground motion: upper continuous traces represent the seismic responses due to the initial basin model, while lower dashed traces are the responses coming from a local rise of 2.5 km of point A. In both cases, the input motion (d) is computed from the record at station 076MZ (listed in Table 1) from event ep04705 (listed in Table 2).

Table 1
Stations and profiles used in this study

No.	Cross section A-A′			Cross section B-B′		
	Stations	Longitude	Latitude	Stations	Longitude	Latitude
1	075SC	118.2276	36.3637	069SS	118.3308	36.3763
2	076MZ	118.2358	36.4600	070WJ	118.3746	36.4481
3	077MZ	118.2285	36.5799	071TJ	118.3226	36.5621
4	078MZ	118.2681	36.6429	072WL	118.3210	36.6250
5	088NW	118.2007	36.7380	087SZ	118.3303	36.7402
6	096LS	118.2278	36.8344	095QD	118.3681	36.8310
7	102ZK	118.2249	36.9061	101QD	118.3448	36.9123
8	114ZH	118.2412	37.0949	107SZ	118.3441	37.0199
9	120YF	118.2572	37.1940	113YZ	118.3514	37.1025
10	126CH	118.2375	37.2924	119YF	118.3626	37.1943
11	132QZ	118.2468	37.3722	125XF	118.3672	37.2710
12	144LJ	118.2297	37.5498	131LJ	118.3319	37.3748
13	–	–	–	137HJ	118.3643	37.4576
14	–	–	–	143SL	118.3673	37.5289
Sect.	A	118.2355	36.3547	B	118.3456	36.3547
	A′	118.2355	37.5687	B′	118.3456	37.5687

could be well constrained by the observed seismic data. At each station, the waveform misfit of the radial component is greater than that of the vertical component while the time residuals of the two components are uniform. This implies that the waveform misfit provides a more important constraint than the travel time residual. An obvious advantage of a lesser waveform misfit of the vertical component and the same time residual of the two components at each station is that we can estimate the time residual by comparing the vertical motion component with the observed record, and then calculate the waveform misfit of the two components.

There exists a linear relationship between misfits and heights when the rise is less than 1.5 km (Fig. 5a). Average increments of 0.6 s in time residual and of 1.9 in waveform misfit per kilometer of local rise within a width of 10 km indicate that linear inversion can be continued in a correct conjugate direction. When the height of a local rise exceeds 1.5 km, the waveform misfit takes a large value and becomes arbitrary. This suggests a non-linear method such as simulated annealing to seek for a model as input for linear inversion.

In addition, maintaining the layer control points and gradually increasing the velocity contrast from 1:1 to 1:4 varying the S-wave velocity in the upper layer, we review the waveform variety. The respective curves of the time residual and the waveform misfit are shown in Fig. 5e. As an example, Fig. 5f shows the seismic response difference at each station with a velocity contrast of 1:2.5. As can be seen, the velocity contrast affects strongly the seismic response of the basin-edge structure. This implies that an initial model with previous geological information is required.

Table 2
Parameters of teleseismic events used in this study

No.	Events	yy-mm-dd	h-m-s	Longitude	Latitude	Depth (km)	M_w
1	ep04705	2001-02-16	05-59-09	117.49	−7.16	521.0	6.1
2	ep05507	2001-02-24	07-23-48	126.25	1.27	35.0	7.1
3	ep07805	2001-03-19	05-52-15	128.02	−4.03	33.0	6.5
4	ep12304	2001-05-03	04-31-57	126.30	0.46	33.0	5.8
5	ep21301	2001-08-04	01-44-53	127.00	2.81	33.0	5.9
6	ep22113	2001-08-09	13-20-17	120.72	−7.35	33.0	5.5
7	ep23901	2001-08-27	01-16-47	126.36	1.09	33.0	6.1

2.4. Full procedure

From Eq. (8) the input motion can be determined from the records observed at a hard rock station over a homogeneous region. We characterize the 2D basin-edge model as a vector **m** with its elements being S-wave velocity and Poisson ratio for every layer, together with the positions of the control interface points. We can thereby introduce the forward modeling operator in the FD scheme for P-SV wave propagation

$$A(\mathbf{m}) = f_{syn}(t), \qquad (14)$$

where A is the forward modeling operator, $f_{syn}(t)$ is the synthetic seismogram, and $\mathbf{m} \in M$, where M represents a L_2-norm Hilbert space of model parameters.
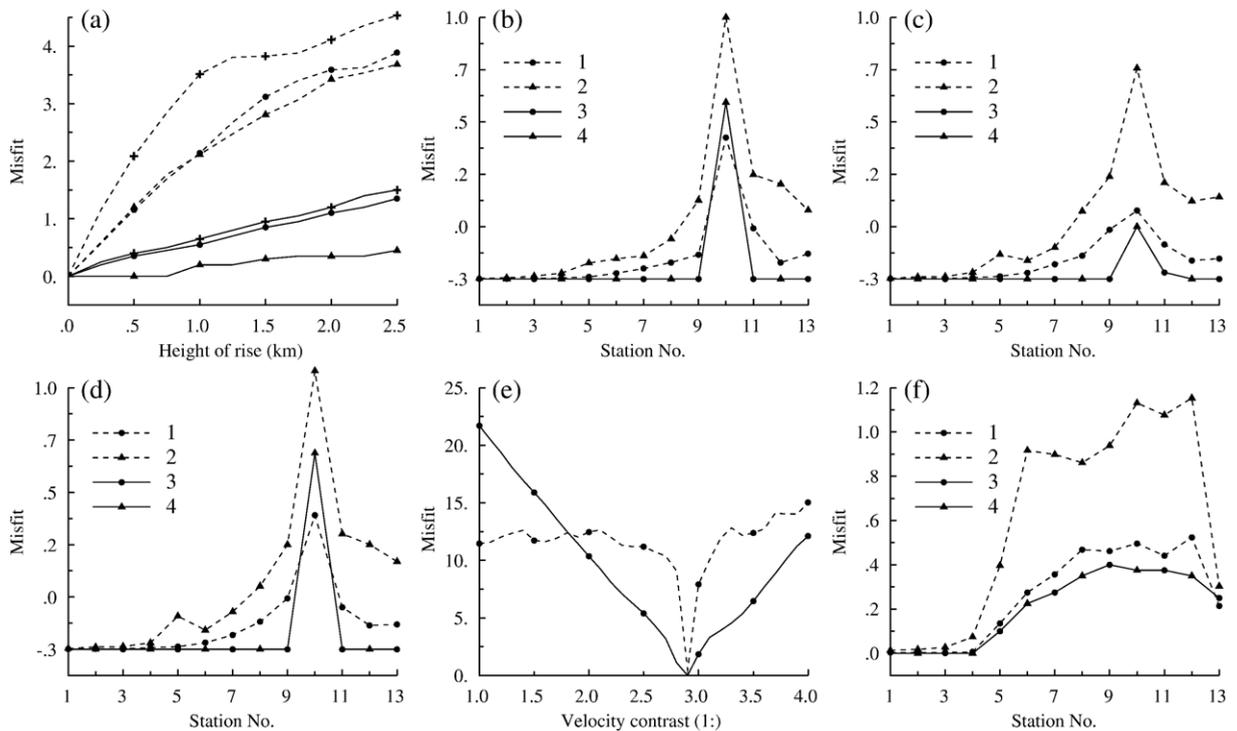

Fig. 5. Numerical experiments displaying the seismic responses in time and waveform due to local changes of the model parameters that configure the hypothesized structure (Fig. 4a). (a) Time residuals (solid lines) and waveform misfits (dashed lines) versus the height of control depth points: black points refer to a rise of 2.5 km of point A, triangles to equal displacement of point B and crosses to equal displacement of both points A and B. (b) Time residuals and waveform misfits obtained for the ground motion vertical and radial components registered at every seismic station after a shift of 2.5 km of point A. Curves 1 and 2 give the waveform misfit whereas curves 3 and 4 give the time residual for the vertical and radial components of the motion, respectively. (c) Analogous results in the case of a shift of 2.5 km of point B. (d) Results obtained when both points A and B are lifted 2.5 km up. (e) Time residual curve (solid line) and waveform misfit curve (dashed line) obtained by keeping the original positions of the layer points (i.e. the geometry of the basin) and varying the S-wave velocity contrast between sedimentary layer and basement. (f) Waveform misfit curves (dashed lines) for the vertical (1) and radial (2) components of the motion, and time residual curves (solid lines 3 and 4) obtained at every seismic station in the case of a velocity contrast of 1:2.5.

Considering the travel time residual $\delta\tau$ and the minimal related coefficient $g(\delta\tau)$, we introduce an object function to measure the difference between observed and synthetic seismograms:

$$O(\mathbf{m}) = W_t \cdot \sqrt{\frac{1}{2N}\sum_{i=1}^{2N}\delta\tau_i^2} + W_f \cdot \sqrt{\frac{1}{2N}\sum_{i=1}^{2N}g_i^2(\delta\tau_i)}, \tag{15}$$

where W_t and W_f are weights for the travel time residuals and the waveform fit, respectively, and are chosen according to the data quality. $2N$ is the number of

vertical and radial waveforms at N stations. The misfit function formalism as shown by Eq. (15), introduced by Luo and Schuster (1991), has a higher resolving ability in waveform inversion (Ji et al., 2000; Zhao et al., 2004). It fails, however, if the initial model is too far away from the real one. Therefore, it is necessary to incorporate a priori knowledge about geological structures for the stability of the inversion. Furthermore, the first term on the right side of Eq. (15) is related to the travel time information and will greatly increase the inversion robustness.

We have developed a sequential waveform method that combines both global and local optimization techniques. Based on experience, we determine the range of the parameters defining the model $\mathbf{m}$. We then use simulated annealing (Ingber, 1989) to minimize the object function given in Eq. (15). A better basin-edge model is created that can be used as the initial model for local optimal process. The conjugate gradient algorithm (Polak, 1971; Ji et al., 2000) is employed to optimize the model. In the FD calculation for P-SV wave propagation, the input motion forms and the incidence angles are different for various selected seismic events. We apply a parallel computation scheme by Tang et al. (1998) to improve the computation efficiency, which allows us to compute synthetic seismograms from different seismic events and the same model in multiprocessor. The full procedure of the sequential waveform method is illustrated by a flow chart as shown in Fig. 6. The initial, annealing and iteration processes are clearly separated and give an overall view of the computation work.

3. Probed region and data acquisition

The Jiyang depression is one of the six main sub-basins in the Bohai Bay Basin Province Eastern China. Lying to the southeast of the basin, it developed during Cenozoic extensional tectonics of the North China Plate. The basin-edge structure is composed of the mountains of the Luxi uplift and the Jiyang depression (Fig. 7a). As a Mesozoic Cenozoic sedimentary depression with abundant oil and gas (Liu and Yang, 1995), the Jiyang depression is composed from bottom to top of the Precambrian crystalline basement, a series of older pre-rift strata, the Tertiary strata and the Quaternary sediments. There is an unconformable contact between any two strata and the dominant lithologies in the Jiyang depression are clastic rocks (Allen et al., 1997).

Data were collected from November 2000 to July 2001. A total of 65 portable broadband stations with CMG-3ESP sensors and REFTEK-72A data acquisition
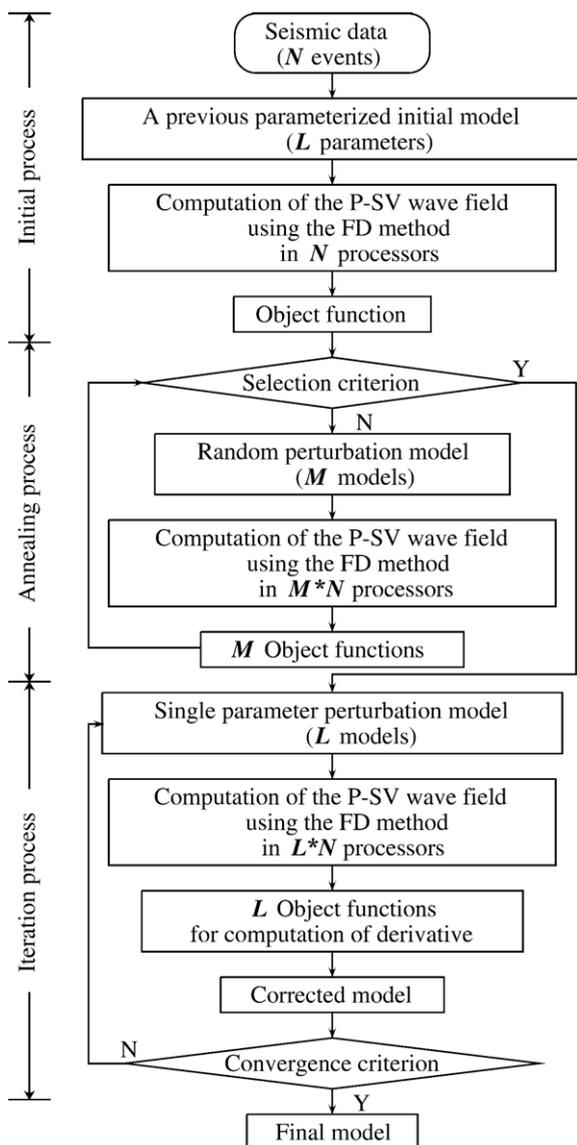

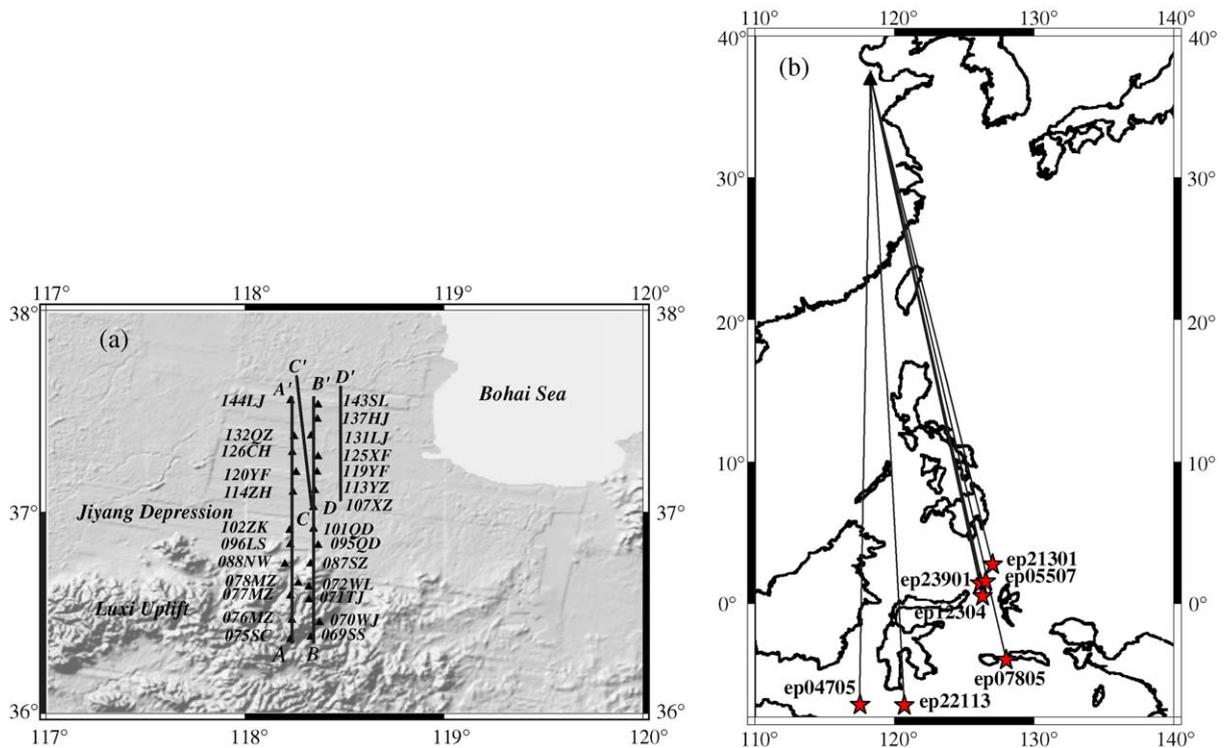Fig. 6. Flow chart of the proposed sequential waveform method.

Fig. 7. (a) Geographical location of the study region and broadband seismic stations installed in the area along parallel profiles A-A′ and B-B′. The segments C-C′ and D-D′ represent two known cross sections that are used for further comparison. (b) Earthquake epicenters (stars) used in this study and source-station paths (straight lines).

systems were deployed on the east part of the Bohai Bay Basin Province. The 26 stations used in this work are shown in Fig. 7a. These stations were installed along two parallel lines crossing the south boundary of the Bohai Bay Basin and covering from south to north the Luxi uplift and the Jiyang depression. The average gap between two adjacent stations is about 10 km. The data are used to constrain the models along two cross sections. We extended 1.0 km from the two terminal stations and built two cross section models named as A-A′ and B-B′ (Fig. 7a). The coordinates of the stations and the profiles are listed in Table 1. We selected seven seismic events whose locations determine almost the same azimuth along the two profiles A-A′ and B-B′ (Fig. 7b). Table 2 lists the earthquake parameters and their magnitudes M_w, which are all ≥5.5. Event locations and origin times are taken from the United States Geological Survey (USGS) catalog.

The seismic data are band pass filtered between 0.02 and 1.0 Hz, and the instrument responses are removed. As an example, Fig. 8 shows the observed seismograms generated by event ep04705 (Table 2). The basin effects in these data are obvious. All the vertical and radial ground motion components show the scale effect of

basin structures on wave propagation. In particular, the amplitude in the vertical components at the basin stations is clearly enhanced. Another remarkable feature is that the traces in the radial components at the basin stations exhibit weak direct arrivals but strong reflected phases, which become stronger at the stations in the deeper basin. We calculated the average incidence angles of the plane wave generated by a teleseismic event at the two extreme points of any profile by the ray parameter. These angles together with the respective epicentral distances and back azimuths are listed in Table 3a and b.

Seismic exploration experiments suggested eight major seismic reflectors in the basin (Wang and Qian, 1992). Following Zhao et al. (2004), we divided our basin model into four major velocity layers, corresponding to Quaternary, Neogene, Paleogene and Pre-Tertiary strata, respectively. The shear velocities, the V_p/V_s ratios and the average densities of the four strata are obtained from drilling core and sonic data (Zhao et al., 2004). The average shear velocity and the V_p/V_s ratio of the basement rock are assigned to be 3.18 km/s and 1.73, respectively (Lu, 1993). Table 4 lists the velocity ranges and the average densities of the five strata.

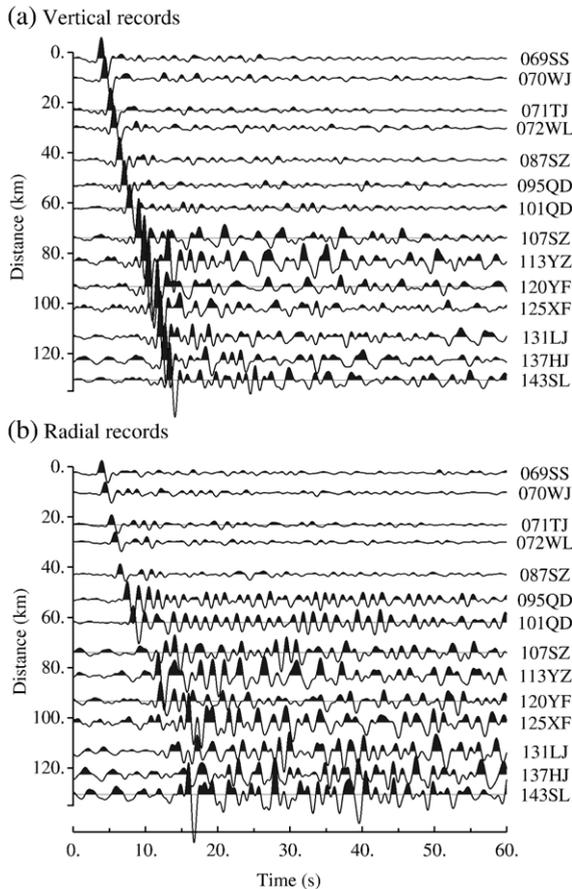(a) Vertical records

(b) Radial records

Fig. 8. Observed seismograms generated by event ep04705 (Table 2) and recorded at the stations (labeled on the right of each waveform) belonging to the profile B-B′. The traces represented in the upper part (a) provide the vertical ground motion, while those plotted in the lower part (b) give the radial ground motion. Clear basin effects can be observed.

Based on the station elevation data, the topographic correction was carried out with the P-wave velocity V_B of the basement rock:

$$\Delta t = -h \cdot \cos\theta / V_B, \qquad (16)$$

where Δt is the value of the correction by topography; h indicates the vertical distance from the observation spot to the datum line; θ is the incidence angle.

4. Results

We have calculated the seismic responses of the southern edge structure of the Bohai Bay basin using the FD method for 2D P-SV elastic wave extrapolation. Along two independent cross sections A-A′ and B-B′,

the length and depth of our model are 135.0 km and 8.0 km, respectively. Four series of the equispaced points divide the basin-edge model into five partitions corresponding to the geological strata. The horizontal spacing between control depth points of the basin models is 5.0 km. The FD calculations have been performed with the grid and time steps $\Delta x = \Delta z = 0.2$ km and $\Delta t = 0.025$ s.

In the annealing process, the control points in each stratum play another role as the upper limits for the last stratum points and the lower threshold for the next layer points. Considering the prior geological information including the drilling data and inferable results from the geological cross sections (Lu and Qi, 1997; Lou et al., 2003), we have estimated that the possible maximum depth of the Neogene stratum is 2.6 km and the possible maximum thickness of the Pre-Tertiary is 3.0 km. These are additional constraint conditions for model reconstructing. Fig. 9a shows an initial basin-edge geometry and physics, where the dashed line represents the upper limit of the basement depth from a priori geological information.

Based on the initial basin model, we have calculated the seismic responses for seven events using seven processors simultaneously. The object function is obtained by comparative analysis of the waveforms. Ten random models are reconstructed to meet the constraint conditions, upon which the forward calculations are performed in seventy processors for the selected seismic events. The ten object functions are obtained simultaneously and compared to determine the optimum one. Considering a laterally homogeneous medium, we smoothed the point depths after the random model is made. The optimum basin-edge models for the two cross sections A-A′ and B-B′ as derived by the simulated annealing method can be seen in Fig. 9b and c, respectively, which are the initial models for the linear iteration process by the conjugate gradient algorithm. Because of the epicenter and azimuth differences for the seven events used in this study and of noise involved, there are some deviations between the observations and the synthetic seismograms. The object functions were found to be 0.58 and 0.69 for the two cross sections A-A′ and B-B′, respectively. The final results are shown in Fig. 10a and c. As an example, the comparison of the observations (solid lines) and the synthetic waveforms (dashed lines) from the earthquakes ep05507 and ep07805 is shown in Fig. 11. It is important to note that, although the recordings at the hard rock stations as the input motions for FD calculation are quite different for the two events, the modeled seismic

Table 3
a) Epicentral distance, back azimuth and incidence angle at the end points of section A-A′

No.	Events	Epicentral distance, km			Back azimuth, degrees			Incident angle, degrees		
		To A	To A′	Aver.	To A	To A′	Aver.	To A	To A′	Aver.
1	Ep04705	4839.5	4974.5	4907.0	181.0	181.0	181.0	23.5	23.2	23.4
2	Ep05507	4001.9	4133.6	4067.8	167.1	167.5	167.3	25.1	24.9	25.0
3	Ep07805	4620.7	4752.0	4686.4	166.4	166.8	166.6	23.9	23.7	23.8
4	Ep12304	4091.0	4222.8	4156.9	167.3	167.7	167.5	24.9	24.7	24.8
5	Ep21301	3855.4	3986.1	3920.8	165.4	165.8	165.6	25.3	25.1	25.2
6	Ep22113	4867.8	5002.6	4935.2	176.7	176.8	176.8	23.4	23.2	23.3
7	Ep23901	4024.2	4155.8	4090.0	167.0	167.4	167.2	25.0	24.8	24.9

b) Epicentral distance, back azimuth and incidence angle at the end points of section B-B′

No.	Events	Epicentral distance, km			Back azimuth, degrees			Incident angle, degrees		
		To B	To B′	Aver.	To B	To B′	Aver.	To B	To B′	Aver.
1	Ep04705	4839.8	4974.7	4907.3	181.1	181.1	181.1	23.5	23.2	23.4
2	Ep05507	3999.2	4131.0	4065.1	167.3	167.7	167.5	25.1	24.9	25.0
3	Ep07805	4617.8	4749.2	4683.5	166.5	166.9	166.7	23.9	23.7	23.8
4	Ep12304	4088.3	4220.2	4154.3	167.5	167.9	167.7	24.9	24.7	24.8
5	Ep21301	3852.3	3983.2	3917.8	165.5	166.0	165.8	25.3	25.1	25.2
6	Ep22113	4867.1	5001.9	4934.5	176.9	177.0	177.0	23.5	23.2	23.4
7	Ep23901	4021.4	4153.2	4087.3	167.2	167.6	167.4	25.0	24.8	24.9

responses fit the observations quite well in times and waveforms, which proves the robustness and reliability of the methodology.

Our results demonstrate that (1) the southern edge of the Jiyang depression begins at ∼40 km from the origin of the profiling, where the waveform amplitudes are enhanced northward to the stations 096LS and 095QD (Fig. 7a), inferring the scale effect of the basin structure on seismic propagation; (2) three hidden faults are revealed to be located at ∼85 km, ∼95 km and 115–125 km; and (3) the basement arises beyond ∼125 km. The observed and calculated seismograms (Fig. 11) are fitted quite well in times and waveforms. The major differences in waveforms come from the radial components of the recordings at stations 125XF, 131LJ and 137HJ. It is to be noted that the cross section A-A′ has apparently a thinner Paleogene formation and a thicker Pre-Tertiary formation than B-B′, which is in agreement with the results published by Zhao et al. (2004).

Table 4
S-wave velocity, Poisson ratio and average density values assigned to the stratified sedimentary materials

Strata	V_s (km/s)	V_p/V_s	ρ (kg/m³)
Quaternary (Q)	0.58–0.62	2.10–2.30	1700.0
Neogene (N)	1.23–1.27	1.72–1.80	2200.0
Paleogene (E)	1.68–1.72	1.70–1.72	2400.0
Pre-Tertiary (P-T)	2.18–2.22	1.42–1.48	2500.0
Basement (B)	3.18 (fixed)	1.73 (fixed)	2800.0

5. Discussion

To evaluate our results we have compared our final models with two known geological cross sections (Fig. 10b and d). The locations of the four cross sections within the study area are indicated by the lines shown in Fig. 7a. As can be seen the line C-C′ (Zhai et al., 1988) locates between A-A′ and B-B′, while the right-hand line D-D′ (Lou et al., 2003) is parallel to our profiles. However, the cross sections C-C′ and D-D′ are somewhat prolonged in the north and shortened in the south. Overall, our models (Fig. 10a and c) are rather similar to the geological cross sections (Fig. 10b and d) in that: (1) both display the "half graben" fault basin type in the Jiyang depression; (2) both extend down to a depth of ∼6.5 km and the Tertiary formations are their major reservoirs; (3) faulting features exist at depth at positions ∼95 km distant from the origin point; and (4) the basin becomes gradually thinner toward the Chenjiazhuang rise (③ in Fig. 10) at about ∼125 km from the model origin.

The fault geometries suggest that the arrays of half grabens are developed on the planar faults of the basement, displaying a typical style of extension. This indicates that the extension plays an important role in the evolution of the Jiyang depression. Based on the geometrical configuration of faults and strata, we infer that the major Cenozoic extension occurred at the Paleogene and finished at the end of the Paleogene (Allen et al., 1997). Although the extension continues at
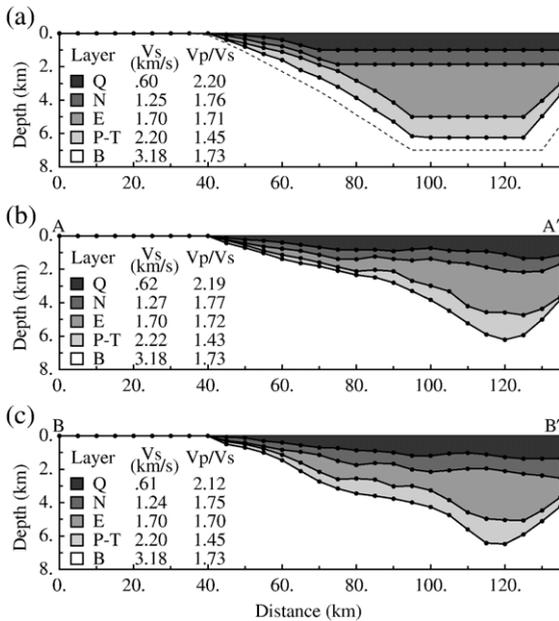
Fig. 9. (a) The initial model of the Jiyang depression constructed from prior geological information including drilling core data and cross sections data. The model consists in four layers of irregular topography overlaying the basement. From top to bottom: Quaternary sedimentary lid (Q), Neogene cover (N), Paleogene layer (E), Pre-Tertiary stratum (P-T) and Precambrian crystalline basement (B). The basin-edge model is parameterized by layer S-wave velocity (V_s) and Poisson ratio. Black points horizontally spaced 5.0 km are control depth points defining the interfaces that configure the geometry of the model. The dashed line is the upper limit of the basement depth fixed by a priori geological information. (b and c) The two parameterized structures inserted in the lower panels are the optimum basin-edge models obtained by simulated annealing, which depict the cross sections A-A′ and B-B′ (Fig. 7a) and are the initial models to start the last step of the computation process (the linear iteration process, Fig. 6) by the conjugate gradient algorithm.

Fig. 10. Final outputs for cross sections A-A′ (a) and B-B′ (c) with layers defined by S-wave velocity and Poisson ratio values. Same legend for materials as in Fig. 9. In these cross sections, the dashed segments represent the inferred hidden faults in the area. Two geological cross sections, C-C′ (b) (after Zhai et al., 1988) and D-D′ (d) (after Lou et al., 2003), are included for comparison. Note that the Quaternary (Q) and Neogene (N) formations are now merged as a single N+Q layer, and that the segments indicate major faults. The south-edge structure of the Jiyang depression appears here formed by Luxi uplift ①, Dongying sag ② and Chenjiazhuang rise ③.

the Neogene and the Quaternary, the amount of extension decreases significantly. As a result, the Neogene stratum has a greater sedimentary range than the Paleogene stratum. Tertiary strata resting unconformably on the Pre-Tertiary rocks form the major reservoir, with the largest thickness that we calculate of about 4.0 km beneath the Dongying sag (② in Fig. 10). The Pre-Tertiary sediments of strongly varying thickness, deposited on the basement during the Upper Jurassic and Lower Cretaceous (Li and Lu, 1988), have undergone strong weathering, erosion and solution since its contact with the Tertiary strata is unconformable. The basement
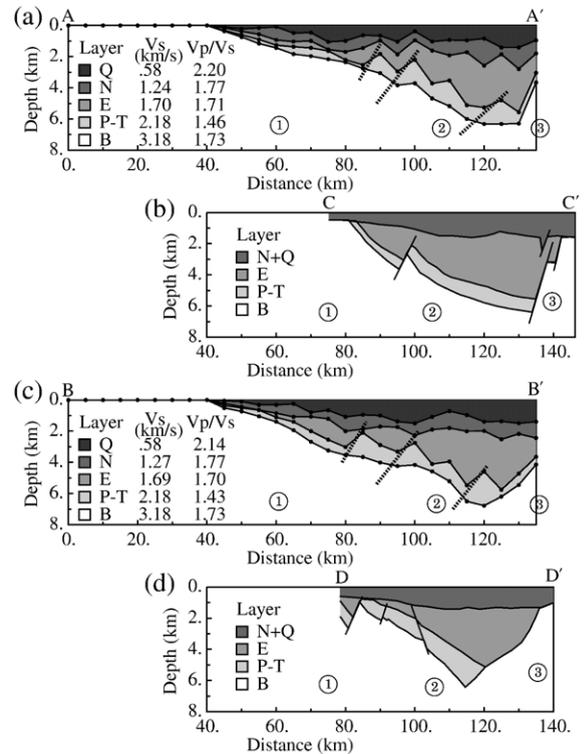
is characterized in shape by step-like structures, and its fractures are attributed to the effect of extensions. The unconformity on the basement implies that the rocks have undergone weathering, erosion and solution.

Comparing our models with the geological cross sections, there still exist somewhat distinctions: (1) there are no faults along the smooth interfaces of the simplified geological sections C-C′ and D-D′ in the Dongying sag, but our results show however the existence of the faults (∼115 km); (2) our longer sections demonstrate that the south boundary of the Jiyang depression against the Luxi uplift begins at

Fig. 11. Observed waveforms (upper continuous traces) from earthquakes ep05507 and ep07805 (2 and 3 as listed in Table 2) compared with the synthetic seismograms (lower dashed traces) obtained from the final basin models shown in Fig. 10a and c. Profiles and stations are properly labeled. The respective input motions for FD calculations (included on top of each comparison) are extrapolated from vertical component records at hard rock stations.
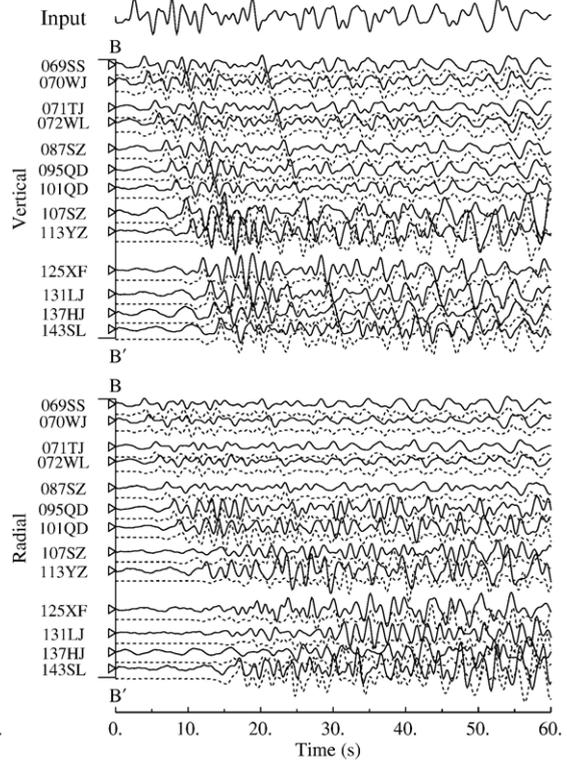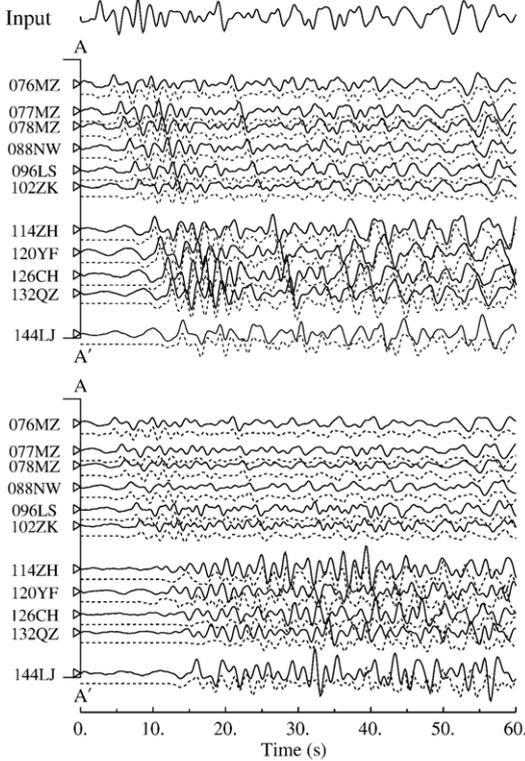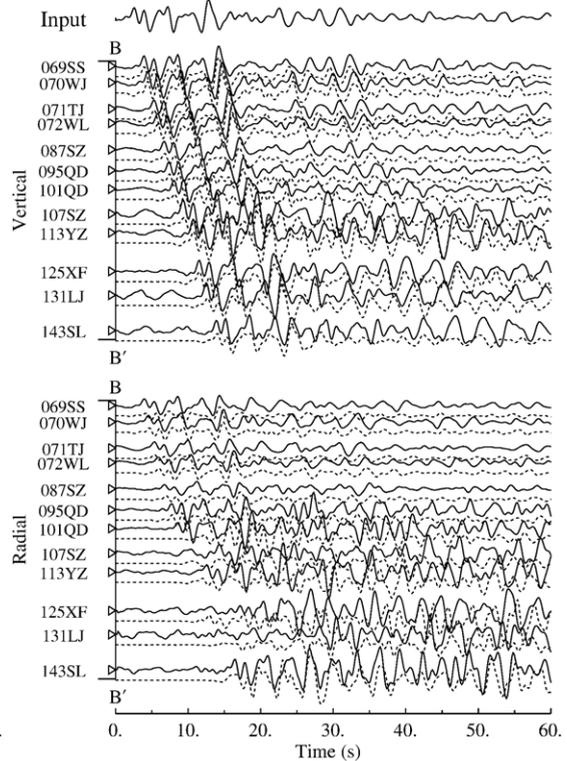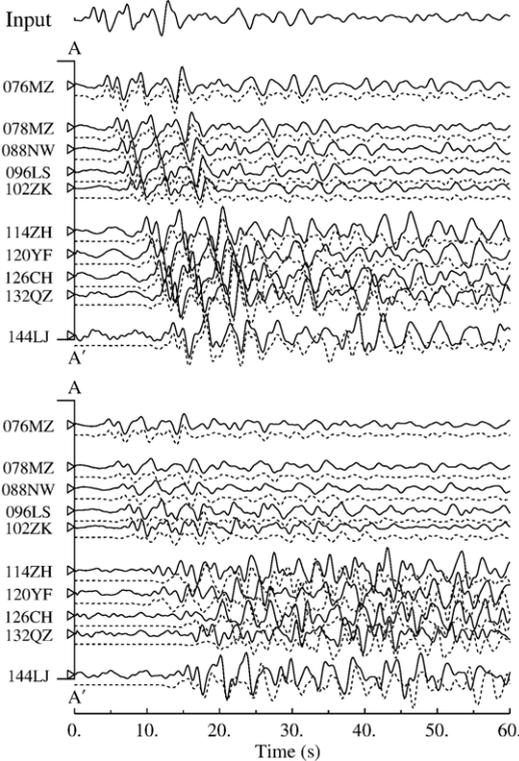
~40 km from the profile origin; and (3) there still exist the Pre-Tertiary strata deposited in the stage of the Chenjiazhuang rise.

6. Conclusions

We have developed a sequential waveform method to model the seismic response of a basin-edge structure. The two-dimensional P-SV elastic wave field has been computed by the FD method, and the simulated responses are compared with the observed teleseismic data to estimate the basin structure. The sequential waveform method consists of the initial, annealing and iterative processes. The computation of the P-SV wave field using the FD method plays an important role in each of these processes. As the seismic attenuation was not taken into account, the input motion can be extrapolated from the coseismic displacement recorded at a hard rock station over the homogeneous region. Numerical tests prove the validity of forward synthetic calculations with a plane wave input motion, and to the resolution and sensitivity of the proposed procedure. Combining simulated annealing and the conjugate gradient algorithm, we are able to investigate the Jiyang depression in the Bohai Bay basin, North China, based on the teleseismic data from seven events. The excellent performance implies the validity of the sequential waveform method.

Although the input motions are not uniform, our results show a good agreement between the recording data and the synthetics, and also with the structural features provided by geology. They imply that the boundary between the Jiyang depression and the Luxi uplift is at ~40 km from the origin of our profiles, and the existence of three hidden faults at ~85 km, ~95 km and 115–125 km. In addition, our results reveal that the south-edge of the Jiyang depression extends northward down to a depth of ~6.5 km in the Dongying sag. The maximum depths in the two studied cross sections are 6.45 and 6.62 km, respectively. The overall configuration displays a step-like extension, which seems to be defined by a series of distinct faults. The faulting geometry suggests that major extensions occurred at the Paleogene and finished at the end of the Paleogene. The Tertiary strata form the major reservoir rocks of the depression.

The teleseismic waveforms recorded in the sedimentary basins are slightly affected by the three-dimensional structure of the basin (Scrivner and Helmberger, 1994). The fact that we have computed the seismic responses for seven events with slightly different azimuths and obtained similar basin-edge models, suggests that our 2D approach is reasonable. Furthermore, if more stations were deployed within the target areas and more calculation resources were used, we should be able to extend our method to 3D modeling of the basin structure.

References

Aio, S., Iwata, T., Irikura, K., Sánchez-Sesma, F.J., 1995. Waveform inversion for determining the boundary shape of a basin structure. Bull. Seismol. Soc. Am. 85, 1445–1455.

Aio, S., Iwata, T., Fujiwara, H., Irikura, K., 1997. Boundary shape waveform inversion for two-dimensional basin structure using three-component array data of plane incident wave with an arbitrary azimuth. Bull. Seismol. Soc. Am. 87, 222–233.

Allen, M.B., Macdonald, D.I.M., Zhao, X., Vincent, S.I., Brouet-Menzies, C., 1997. Early Cenozoic two-phase extension and late Cenozoic thermal subsidence and inversion of the Bohai Basin, northern China. Mar. Pet. Geol. 14, 951–972.

Anderson, J.G., Bodin, P., Brune, J.N., Prince, J., Singh, S.K., Quaas, R., Onate, M., 1986. Strong ground motion from the Michoacan, Mexico, earthquake. Science 233, 1043–1048.

Beck, J.L., Hall, J.F., 1986. Factors contributing to the catastrophe in Mexico City during the earthquake of September 19 1985. Geophys. Res. Lett. 13, 593–596.

Campillo, M., Gariel, J.C., Aki, K., Sánchez-Sesma, F.J., 1989. Destructive strong ground motion in Mexico City: source, path, and site effects during great 1985 Michoacan earthquake. Bull. Seismol. Soc. Am. 79, 1718–1735.

Chávez-García, F.J., 2003. Site effects in parkway basin: comparison between observations and 3-D modeling. Geophys. J. Int. 154, 633–646.

Chávez-García, F.J., Stephenson, W.R., Rodriguez, M., 1999. Lateral propagation effects observed at Park way, New Zealand. A case history to compare 1D vs. 2D site effects. Bull. Seismol. Soc. Am. 89, 718–732.

Clayton, R.W., Engquist, B., 1977. Absorbing boundary conditions for acoustic and elastic wave equations. Bull. Seismol. Soc. Am. 67, 1529–1540.

Duggan, E.B., 1997. Shallow seismic structure of Parkway basin, Wainuiomata, New Zealand. BSc. (Hons) thesis, Victoria University of Wellington, New Zealand.

Hauksson, H., Haase, J., 1997. Three-dimensional V_p and V_p/V_s in the Los Angeles basin and central Transverse Ranges, California. J. Geophys. Res. 102, 5423–5454.

Hou, G.T., Qian, X.L., Cai, D.S, 2001. The tectonic evolution of Bohai Basin in Mesozoic and Cenozoic time. Acta Sci. Nat. Univ. Pekinensis 37 (6), 845–851 (in Chinese).

Ingber, L., 1989. Very fast simulated re-annealing. Math. Comput. Model. 12, 967–973.

Ji, C., Helmberger, D.V., Wald, D., 2000. Basin structure estimation by waveform modeling: forward and inverse methods. Bull. Seismol. Soc. Am. 90, 964–976.

Jongmans, D., Pitilakis, K., Demanet, D., Raptakis, D., Riepl, J., Horrent, C., Tsokas, G., Lontzetidis, K., Bard, P.-Y., 1998. EURO-SEISTEST: determination of the geological structure of the Volvi basin and validation of the basin response. Bull. Seismol. Soc. Am. 88, 473–487.

Kawase, H., Aki, K., 1989. A study on the response of a soft basin for incident S, P, and Rayleigh waves with special reference to the long duration observed in Mexico City. Bull. Seismol. Soc. Am. 79, 1361–1382.

Kebeasy, T.R.M., Husebye, E.S., 2003a. A finite-difference approach for simulating ground responses in sedimentary basin: quantitative modeling of the Nile Valley, Egypt. Geophys. J. Int. 154, 913–924.

Kebeasy, T.R.M., Husebye, E.S., 2003b. Revising the 1759 Kattegat earthquake questionnaires using synthetic wave field analysis. Phys. Earth Planet. Inter. 139, 269–284.

Langston, C.A., 1977. Corvallis, Oregon, crustal and upper mantle receiver structure from teleseismic P and S waves. Bull. Seismol. Soc. Am. 67, 713–724.

Langston, C.A., 1979. Structure under Mount Rainer, Washington, inferred from teleseismic body waves. J. Geophys. Res. 84 (B9), 4749–4762.

Li, G., Lu, M., 1988. Atlas of Oil and Gas Basins in China. Petroleum Industry Publishing House, Beijing, China (in Chinese).

Liu, Q.Y., Kind, R., Li, S.C., 1996. Maximal likelihood estimation and nonlinear inversion of the complex receiver function spectrum ratio. Chin. J. Geophys. 39 (4), 502–513 (in Chinese).

Liu, X., Yang, S., 1995. Exploration theory and method in Jiyang composite oil and gas area. China Oil Gas 2, 20–22 (in Chinese).

Lou, Z.H., Zhu, R., Jin, A.M., Wu, H.Z., Zheng, H.R., Wang, N., 2003. Formation and evolution of hydrodynamic field in the Dongying depression. Chin. J. Geol. 38 (1), 85–96 (in Chinese).

Lu, J.M., 1993. Principles of Seismic Exploration. Press of Petroleum University, Beijing, China (in Chinese).

Lu, K.Z., Qi, J.F., 1997. Tectonic Model of Cenozoic Petroliferous Basin Bohai Bay Province. Geological Publishing House, Beijing, China (in Chinese).

Luo, Y., Schuster, G.T., 1991. Wave-equation travel-time inversion. Rev. Geophys. 56, 645–653.

Magistrale, H., McLaughlin, K., Day, S., 1996. A Geology-based 3D velocity model of the Los Angeles Basin sediments. Bull. Seismol. Soc. Am. 86, 1161–1166.

Olsen, K.B., Archuleta, R.J., Matarese, J.R., 1995. Magnitude 7.75 earthquake on the San Andreas fault: three-dimensional ground moyion in Los Angeles. Science 270, 1628–1632.

Owens, T.J., Zandat, G., Taylor, S.R., 1984. Seismic evidence for an ancient rift beneath the Cumberland Plateau, Tennessee: a detailed analysis of broadband teleseismic P waveforms. J. Geophys. Res. 89 (B9), 7783–7795.

Polak, E., 1971. Computational Method in Optimization. Academic Press, New York, pp. 44–65.

Riepl, J., Bard, P.Y., Hatzfeld, D., Papaioannou, C., Nechtschein, S., 1998. Detailed evaluation of site-response estimation methods across and along the sedimentary valley of Volvi (EURO-SEISTEST). Bull. Seismol. Soc. Am. 88, 488–502.

Scrivner, C.W., Helmberger, D.V., 1994. Seismic waveform modeling in the Los Angeles Basin. Bull. Seismol. Soc. Am. 85, 1445–1455.

Stephenson, W.R., 2000. The dominant resonance response of Parkway basin. Proc. 12th world Conf. on Earthq. Eng., Auckland, New Zealand, CD-ROM, New Zealand Society for Earthquake Engineering, Paper 1272. 7 pp.

Tang, L.S., Xie, Y., You, S.Y., Luo, Z.H., 1998. Non-Numerical Parallel Algorithm for Simulated Annealing. Science Publishing House, Beijing, China (in Chinese).

Wald, D.J., Graves, R.W., 1998. The seismic response of Los Angeles Basin, California. Bull. Seismol. Soc. Am. 88, 337–356.

Wang, B., Qian, K., 1992. Geologic Research and Exploration in Shengli Oilfield. Press of Petroleum University, Beijing, China (in Chinese).

Wen, L., Helmberger, D.V., 1997. Propagational corrections for basin structure: Landers earthquake. Bull. Seismol. Soc. Am. 87, 782–787.

Wen, L., Helmberger, D.V., 1998. A two-dimensional P-SV hybrid method and its application to modeling localized structures near the core-mantle boundary. J. Geophys. Res. 103 (B8), 17901–17918.

Yamanaka, H., Seo, K., Samano, T., 1989. Effects of sedimentary layers on surface-wave propagation. Bull. Seismol. Soc. Am. 79, 631–644.

Ye, H., Zhang, B.T., Mao, F.Y., 1987. The Cenozoic tectonic evolution of the great North China: two types of rifting and crustal necking in the great North China and their tectonic implications. Tectonophysics 133, 217–227.

Yuan, X., Sobolev, S.V., Kind, R., Oncken, O., Bock, G., Asch, G., Schurr, B., Graeber, F., Rudloff, A., Hanka, W., Wylegalla, K., Tibi, R., Haberland, Ch., Rietbrock, A., Giese, P., Wigger, P., Röwer, P., Zandt, G., Beck, S., Wallace, T., Pardo, M., Comte, D., 2000. Subduction and collision processes in the central andes constrained by converted seismic phase. Nature 408, 958–961.

Zahradník, J., 1995. Simple elastic finite-difference scheme. Bull. Seismol. Soc. Am. 85, 1879–1887.

Zhai, G., Wang, S., Li, G., 1988. Characteristics and oil and gas potential of sedimentary basins of China. In: Wagner, H.C., Wagner, L.C., Wang, F.F.H., and, F.L. (Eds.), Petroleum Geology of China and Related Subjects. Circum-Pacific Council for Energy and Mineral Resources. Earth Science Series, vol. 10, pp. 1–22.

Zhang, Z., Yang, L., Teng, J., Badal, J., in review. Symmetry signature of the crust in China. J. Geophys. Res.

Zhao, L., Zheng, T.Y., Xu, W., 2004. Modeling the Jiyang depression, Northern China, using a wave-field extrapolation FD method and waveform inversion. Bull. Seismol. Soc. Am. 94, 988–1001.